MOLECULAR GAS DYNAMICS OF THE STRONGLY-LENSED WET-MERGER RXS J1131−1231 AT Z=0.654

T. K. Daisy Leung and Dominik A. Riechers

Department of Astronomy, Space Sciences Building, Cornell University, Ithaca, NY 14853, USA; tleung@astro.cornell.edu

To be submitted to the ApJ

ABSTRACT

We present interferometric observations of $CO(J = 2 \rightarrow 1)$ and $CO(J = 3 \rightarrow 2)$ emission toward the "Einstein ring" RXS J1131−1231 at $z = 0.654$, obtained with the Plateau de Bure Interferometer and Combined Array for Research in Millimeter-wave Astronomy. Our observations detect a CO-emitting source near RXJ1131, confirming the presence of an optically faint companion reported in previous studies. Based on our dynamical lens modeling of the spatially and spectrally resolved $CO(J = 2 \rightarrow 1)$ emission, we reconstruct a symmetric velocity gradient in the source plane and find an intrinsically symmetric double-horned line profile, which are suggestive of a rotating disk morphology, consistent with previous optical studies. We find a lensing-corrected gas mass of $M_{gas} \sim 1.4 \times 10^{10} M_\odot$ in the host galaxy and $\sim 2 \times 10^9 M_\odot$ in the companion (gas mass ratio ∼7:1). The CO disk is extended over ∼6 kpc, which yields a dynamical mass of $M_{dyn} \sim 8 \times 10^{10} M_\odot$ for the host galaxy. This corresponds to a gas mass fraction of ∼19%, confirming its gas-rich nature. This fraction also confirms the trend of decreasing gas fraction since $z \sim 1$, which is responsible for the decline of the cosmic star formation rate and black hole accretion rate densities. Fitting dust SED models, we derive a lensing-corrected dust mass of $M_{dust} = 4 \times 10^8 M_\odot$, a lensing-corrected $L_{IR} \sim 1.5 \times 10^{12} L_\odot$, and a $SFR_{FIR} = 120 \pm 63 M_\odot \ yr^{-1}$, confirming the dusty nature of the merger. A comparison of the gas and stellar distributions reveals active starbursts embedded within the molecular gas reservoir which is likely a result from merger-driven gas inflow. The nature of RXJ1131 is consistent with the picture predicted by model simulations, in which it will likely retain its disk component and evolve into small bulge disk galaxy upon merging. Our study presents the first resolved CO imaging at intermediate redshift, which allows us to provide the first dynamical constraint on the $M_{BH} - \sigma_*$ relation at intermediate redshift.

Subject headings: ISM: molecular – infrared: galaxies – galaxies: mergers – galaxies: starburst – galaxies: evolution

1. INTRODUCTION

Studies of galaxy evolution have been focusing on the interplay between baryonic physics/processes (e.g., feedback and gas dissipation) and star formation and active galactic nucleus (AGN) activity across cosmic epochs. It is not well-understood when and how baryons of present-day galaxies were assembled, but it is clear that both the co-moving star formation rate and black hole accretion rate densities increased substantially since $z > 3$ and reached their climax at $z \sim 2$, followed by a rapidly decline toward $z \sim 0$ (e.g., Hopkins & Beacom 2006; Madau & Dickinson 2014). A leading explanation for this decline is related to the evolution of molecular gas content and star formation efficiency (Erb et al. 2006; Carilli & Walter 2013; Walter et al. 2014), but confirmation from direct molecular gas measurements at intermediate redshift ($0.2 < z < 1$) is still limited both in number and in the variety of galaxy populations probed — only unresolved CO observations have been carried out for ∼70 ULIRGs up to date (Combes et al. 2011, 2013).

Meanwhile, empirical scaling relations such as the Magorrian relation (Magorrian et al. 1998) — a tight correlation between black hole mass and stellar bulge mass — have been established locally, implying a self-regulating co-eval growth between local SMBHs and their host galaxies. Attempts to extend this relation out to higher redshifts,

beyond the peak epoch of star formation and AGN activity, have been made in recent years. It has been reported that the M_{BH}/M_{bulge} ratio of high-z submillimeter galaxies (SMGs) falls below the local relation (e.g., Borys et al. 2005; Alexander et al. 2008) but that of high-z quasar host galaxies are found lying above the relation (e.g., McLure et al. 2006; Peng et al. 2006). Stellar mass of quasar host galaxies at $z > 4$ constrained by their CO-based dynamical mass are also too small compared to that based from the local relation (Walter et al. 2004; Riechers et al. 2008; Coppin et al. 2008). While it has become clearer that high-z galaxies deviate from the local relation, and among their galaxy populations, such a picture is still unclear at intermediate redshift. This owes to the difficulties in measuring stellar emission in the host galaxy under the presence of a bright quasar, or alternatively owing to the lack of spatially resolved CO observations to provide dynamical constraints on the stellar mass. With gravitational lensing, emission of the background quasar and its host galaxy is magnified and stretched out to different extents, and is being projected onto different locations in the image plane. This in effect increases the surface brightness contrast between their emission and allows for the relatively uncontaminated measurements of their emission.

The "Einstein ring" RXS J113151.62−123158 (hereafter RXJ1131) at $z_{s, QSO} = 0.685$ (Sluse et al. 2003, hereafter

S03) is a particularly well-suited source for studying the evolution of molecular gas properties in quasar host galaxies and the connection between SMBHs and their host galaxies at intermediate redshift given its unique lensing configuration. The stellar emission in the host galaxy of RXJ1131 is lensed into an Einstein ring of radius $1\overset{''}{.}83$ that is clearly separated from the quadruply imaged quasar emission (Claeskens et al. 2006, hereafter C06). We have thus carried out a detailed study for RXJ1131 as presented in this paper. RXJ1131 is strongly lensed by an elliptical galaxy at $z_L = 0.295$ (S03). The moderate mass black hole $M_{BH} = 8 \times 10^7 M_\odot$ (Sluse et al. 2012) residing in RXJ1131 is rotating with a high spin parameter ($a \sim 0.9$; Reis et al. 2014), and is radiating at an intrinsic bolometric luminosity of $L_{bol,X} = 1.3 \times 10^{45}$ ergs s^{-1} (Pooley et al. 2007).

This paper is structured as follows. In §2, we outline the details of the observations and our data reduction process. In §3, we describe our astrometric corrections applied to align an *HST* image with our radio maps. In §4, we report measurements of the CO($J = 2 \rightarrow 1$) and CO($J = 3 \rightarrow 2$) lines and a compilation of photometric data from optical to radio wavelengths. In §5, we present dynamical lens modeling of the CO($J = 2 \rightarrow 1$) data, SED modeling of the thermal dust continuum, and the resulting physical properties inferred for RXJ1131. In §6, we discuss the merger stage of RXJ1131, the scenario of a recoiling black hole, and the $M_{BH}-M_{dyn}$ relation. Finally, we summarize the main results and present our conclusions in §7. We use a concordance ΛCDM cosmology throughout this paper, with parameters from the WMAP9 results: $H_0 = 69.32$ km s^{-1} Mpc^{-1}, $\Omega_M = 0.29$, and $\Omega_\Lambda = 0.71$ (Hinshaw et al. 2013).

2. OBSERVATIONS

2.1. *PdBI CO($J = 2 \rightarrow 1$)*

Observations of the CO($J = 2 \rightarrow 1$) rotational line ($\nu_{rest} = 230.5379938$ GHz) redshifted to $\nu_{obs} = 139.0$ GHz were carried out using IRAM Plateau de Bure Interferometer (PdBI; Program ID: S14BX; PI: D. Riechers). Two observing runs were carried out on 2014 December 06 and 2015 February 05 under good weather conditions in the C and D array configurations, respectively. The 2 mm receivers were used to cover the redshifted CO($J = 2 \rightarrow 1$) line and the underlying continuum emission, employing a correlator setup that provides an effective bandwidth of 3.6 GHz (dual polarization) and a spectral resolution of 10.0 MHz (~ 21.5 km s^{-1}). This resulted in 3.75 hours of cumulative six antenna-equivalent on-source time after discarding unusable visibility data. The nearby quasars B1127−145 and B1124−186 were observed every 22 minutes for pointing, secondary amplitude, and phase calibration, and B1055+018 was observed as the bandpass calibrator for both tracks. MWC349 and 3C279 were observed as primary flux calibrators for the C and D array observations, respectively, yielding $\lesssim 15\%$ calibration accuracy.

The GILDAS package was used to reduce and analyze the visibility data. The calibrated visibility data were imaged and deconvolved using the CLEAN algorithm with

"natural" weighting. This yields a synthesized clean beam size of $4\overset{''}{.}44 \times 1\overset{''}{.}95$ (PA = 13°). The final rms noise is $\sigma = 1.45$ mJy beam^{-1} over 10 MHz (21.5 km s^{-1}). The continuum image at $\nu_{cont} \sim 139$ GHz is created by averaging over 3.16 GHz of line-free bandwidth. This yields an rms noise of 0.082 mJy beam^{-1}.

2.2. *CARMA CO($J = 3 \rightarrow 2$)*

Observations of the CO($J = 3 \rightarrow 2$) rotational line in RXJ1131 ($\nu_{rest} = 345.7959899$ GHz) redshifted to $\nu_{obs} = 208.6$ GHz were carried out with the Combined Array for Research in Millimeter-wave Astronomy (CARMA; Program ID: cf0098; PI: D. Riechers) in the D array configuration on 2014 February 02 under poor 1.5 mm weather conditions and on 2014 February 17 under good 1.5 mm weather conditions. The correlator setup provides a bandwidth of 3.75 GHz in each sideband and a spectral resolution of 12.5 MHz (~ 17.9 km s^{-1}). The line was placed in the lower sideband with the local oscillator tuned to $\nu_{LO} \sim 216$ GHz. The radio quasars J1127−189 (first track) and 3C273 (second track) were observed every 15 minutes for pointing, amplitude, and phase calibration. Mars was observed as the primary absolute flux calibrator and 3C279 was observed as the bandpass calibrator for both tracks. This results in a total on-source time of 2.94 hours after flagging poor visibility data.

Given that the phase calibrator used for the first track was faint and was observed under poor weather conditions and that the phase calibrator used for the second track was far from our target source, the phase calibration is subpar, with an rms scatter $\sim 60°$ over a baseline length of ~ 135 m. We thus conservatively estimate a calibration accuracy of $\sim 45\%$ based on the flux scale uncertainties, the gain variations over time, and the phase scatter on the calibrated data. We therefore treat its line intensity with caution and ensure that our physical interpretation of this system and the conclusion of this paper do not rely on this quantity.

The MIRIAD package was used to calibrate the visibility data. The calibrated visibility data were imaged and deconvolved using the CLEAN algorithm with "natural" weighting. This yields a synthesized clean beam size of $3\overset{''}{.}2 \times 1\overset{''}{.}9$ (PA = 8°) for the lower sideband image cube. The final rms noise is $\sigma = 13.3$ mJy beam^{-1} over a channel width of 25 MHz. An rms noise of $\sigma = 0.83$ mJy beam^{-1} is reached by averaging over the line-free channels.

2.3. *VLA (Archival)*

Our analysis also uses archival data of the 5 GHz radio continuum obtained with the Very Large Array (VLA; Program ID: AW741; PI: Wucknitz). Observations were carried out on 2008 December 29 under excellent weather conditions in the A array configuration for a total of ~ 7 hours on-source time. The C-band receivers were used with a continuum mode setup, providing a bandwidth of 50 MHz for the two IF bands with full polarization. The nearby radio quasar J1130−149 was observed every 10 minutes for pointing, amplitude, and phase calibration,

J1331+305 was observed as the primary flux calibrator, and J0319+415 was observed as the bandpass calibrator, yielding ∼10% calibration accuracy. We used AIPS to calibrate the visibility data. The calibrated visibility data were imaged and deconvolved using the CLEAN algorithm using robust = 0. This yields a synthesized clean beam size of 0.″49 × 0.″35 (PA = 0.18°) and a final rms noise of $\sigma = 13 \, \mu$Jy beam^{-1}.

3. HST ASTROMETRY

We obtained an *HST* image taken with the ACS/Wide Field Camera using the F555W filter (*V*-band) from the Hubble Legacy Archive[1]. The details of the observations can be found in C06. We adopt the VLA 5 GHz map as the reference coordinate frame to align the optical (*V*-band) image. We shift the latter to the east by 0.″5963 in R.A. and +0.″8372 in Dec., which is consistent with the typical astrometric precision (1″−2″) of images from the Hubble Legacy Archive[2]. This astrometric correction is critical to avoid artificial spatial offsets between different emitting regions and to carry out our lens modeling, in which the absolute position of the foreground lensing galaxy is guided by its coordinates in the high-resolution optical image. The VLA image is calibrated using a well-monitored phase calibrator, with absolute positional accuracy of ∼2 mas. For this reason, the absolute alignment between the VLA image and other interferometric images reported in this paper are expected to have an astrometric precision better than 0.″1, modulo uncertainties related to the SNR and phase instability.

4. RESULTS

4.1. *CO(J = 2 → 1) Emission*

We detect CO($J = 2 \to 1$) line emission toward the background source at $\gtrsim 27\sigma$ significance, confirming the redshift at $z_{CO} = 0.65370 \pm 0.0005$. The emission is spatially and dynamically resolved with a highly asymmetric double-horned line profile as shown in Figure 1. Fitting a double Gaussian results in peak flux densities of 75.3 ± 2.6 and 24.0 ± 2.0 mJy, and a FWHM of 179 ± 9 km s^{-1} and 255 ± 28 km s^{-1} for the two components, respectively. The peaks are separated by $\Delta v_{sep} = 400 \pm 12$ km s^{-1}. The total integrated line flux is 24.1 ± 2.3 Jy km s^{-1}.

We construct the zeroth moment map, a red/blue channel map, and the first and second moment maps in Figure 2 using the *uv*-continuum subtracted data cube over a velocity range of $\Delta v \sim 750$ km s^{-1}. The higher-order moment maps are created using unbinned channel maps with 3σ clipping. The peak flux density is 8.12 ± 0.30 Jy km s^{-1} beam^{-1} in the intensity map.

The deconvolved source size FWHM from fitting a two-dimensional Gaussian is $5.″1 \pm 0.″72 \times 3.″72 \pm 0.″66$, and thus, the emission is resolved over ∼2.2 beams. While
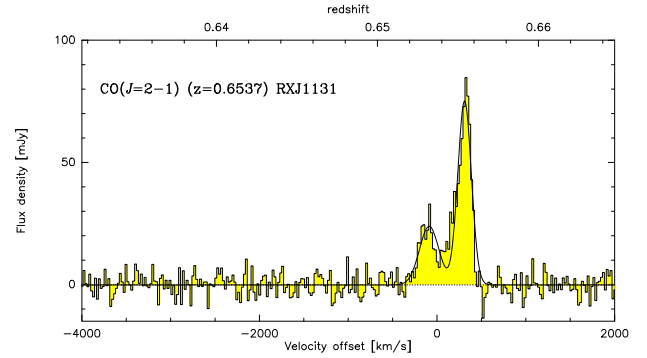
FIG. 1.— Spectrum of CO($J = 2 \to 1$) emission toward RXJ1131. The velocity scale is with respect to $z = 0.6537$, which is approximately the line center considering the asymmetry resulting from differential lensing. A detailed discussion of this effect is presented in §5.1.2.

the lensed emission is not strictly distributed as a two-dimensional Gaussian; the fit recovers the line intensity enclosed by the emitting region, we therefore take this as an estimate on the extent of the lensed emission. On the other hand, if we assume that the spatial distribution of the lensed molecular gas emission is similar to that in the optical to near-IR wavelengths, the lensed emission would be more accurately described by an annulus, enclosing the partially complete "Einstein ring" and the lensed knots (see Figure 2).

We also place an upper limit on HNC($J = 2 \to 1$) line emission in the foreground galaxy at $z \sim 0.295$. Assuming a typical line width of 300 km s^{-1}, this corresponds to a 3σ limit of 0.35 Jy km s^{-1} beam^{-1}.

4.2. *CO(J = 3 → 2) Emission*

We detect CO($J = 3 \to 2$) line emission toward RXJ1131 at **BLAH**σ significance. The spectrum is shown in Figure 3, which appears to be consistent with a double-peaked profile. We estimate a line intensity of 35.7 ± 21.9**BLAH** Jy km s^{-1} by summing up fluxes over the FWZI linewidth used to infer the CO($J = 2 \to 1$) line intensity (∼700 km s^{-1}). Assuming the spatial extent between CO($J = 2 \to 1$) and CO($J = 3 \to 2$) is similar and therefore the emission is magnified by the same amount, the measured line intensities correspond to a brightness temperature ratio of $r_{32} = T_{CO(J = 3 \to 2)} / T_{CO(J = 2 \to 1)} = 0.66 \pm 0.41$. Taking into account the large phase errors associated with CO($J = 3 \to 2$), this is consistent with thermalized excitation, as observed in other ULIRGs.

4.3. *Continuum Emission*

No 1.5 mm continuum emission is detected at the position of CO($J = 3 \to 2$) down to a 3σ limit of 2.49 mJy beam^{-1}. This is consistent with the spectrum shown in Figure 3.

We detect PdBI 2 mm continuum in Figure 4. The integrated flux density is 1.2 ± 0.2 mJy, with a peak flux $S_\nu = 800 \pm 88 \, \mu$Jy beam^{-1} centered on the lensing galaxy. Slightly extended emission is also detected along the lensed arc. This suggests that the detected emission comes from both the foreground galaxy and the background galaxy and that the emission is marginally resolved along
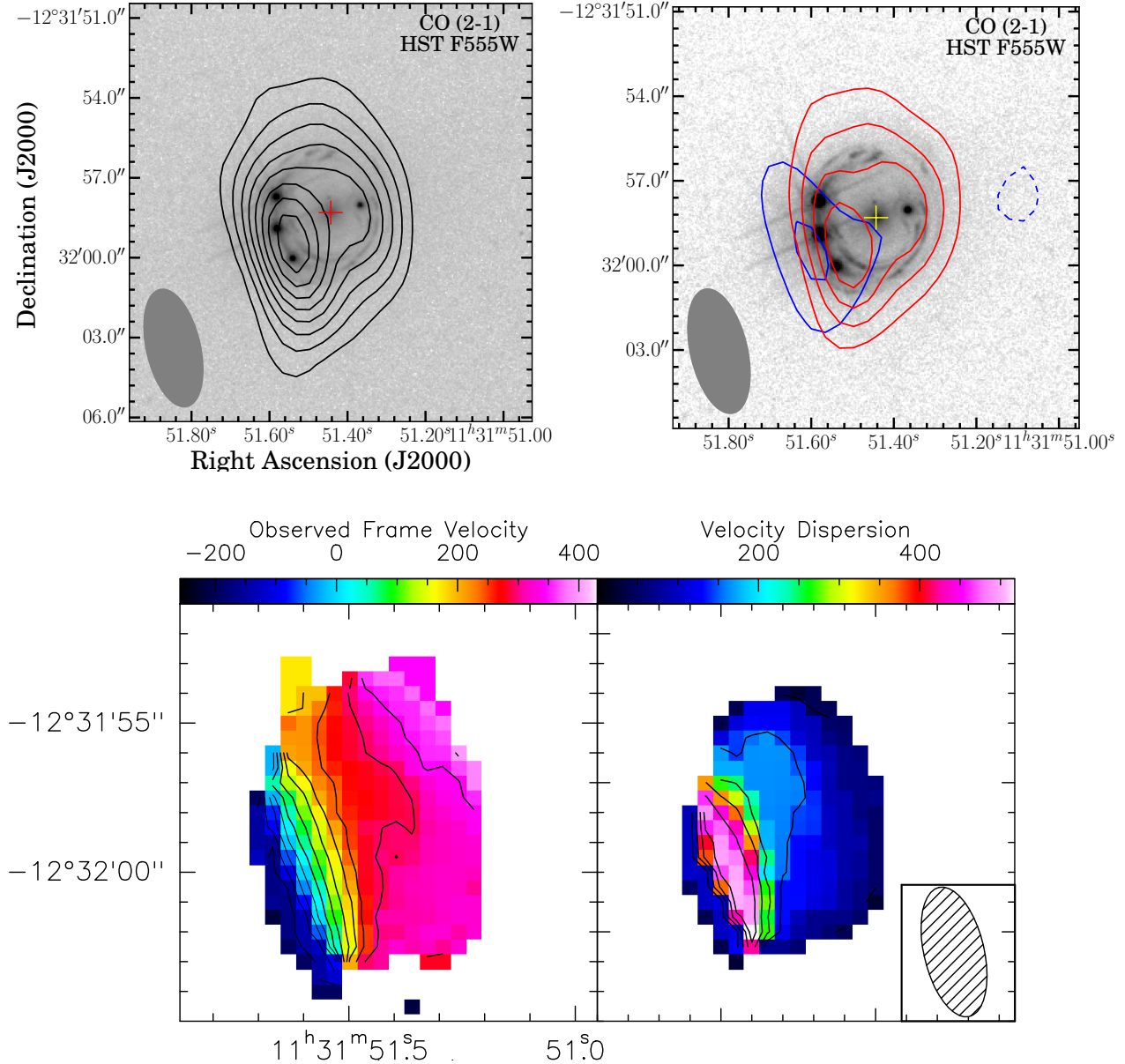
FIG. 2.— Top left: overlay of the velocity-integrated CO($J = 2 \rightarrow 1$) emission on the archival *HST V*-band (F555W) image. Top right: same as top left, except the contours are color-coded to represent the red- and blueshifted emission. The contours in both top panels start at 3σ and increment at steps of $\pm 3\sigma$, where $\sigma = 0.3$ mJy beam^{-1} for the top left panel, and $\sigma = 0.4$ mJy beam^{-1} (red) and 0.5 mJy beam^{-1} (blue) for the top right panel. The crosses denote the location of the foreground galaxy at $z = 0.295$. Contours for the first (bottom left) and second (bottom right) moment maps of the CO($J = 2 \rightarrow 1$) line emission are shown in steps of 50 km s^{-1}, and 100 km s^{-1}, respectively. The synthesis beam size is $4.''4 \times 2.''0$, at PA = 13°.

its major axis. We subtract a point source model in *uv*-plane to remove the unresolved emission toward the foreground galaxy. The peak flux (0.39 ± 0.08 mJy) in the residual map coincides with the lensed arc, and is consistent with the difference between the integrated and the peak flux in the original continuum map (~ 0.4 mJy). We therefore adopt $S_\nu = 0.39 \pm 0.08$ mJy as the 2 mm continuum emission toward the background galaxy (RXJ1131).

The VLA C-band continuum image in Figure 4 shows resolved emission from the jets and the core of the foreground elliptical galaxy as well as emission toward the background quasar. Multiple peaks are seen along the arc with their centroids coincident with the optical emission from the quasar. We extract the flux densities for

the lensing arc and the radio core in Table 1. We find a spectral index of $\alpha_{6cm}^{2mm} = -0.024$ for the foreground galaxy and $\alpha_{6cm}^{2mm} = -0.345$ for the background galaxy by fitting a power-law ($S_\nu \propto \nu^\alpha$) to the continuum emission at 5 GHz and 2 mm.

4.4. *Photometry*

We compile mid-IR (MIR) to far-IR broadband photometry from various catalogs available on the NASA/IPAC Infrared Science Archive (IRSA) in Table 1 with aperture corrections when warranted. These data were obtained using the Two Micron All Sky Survey Telescopes (2MASS; Skrutskie et al. 2006), the Wide-field Infrared Survey Explorer (*WISE*; Wright et al. 2010), the *Infrared Astronomi-*
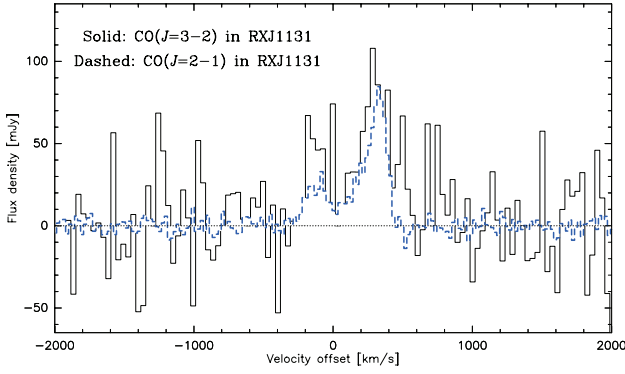
FIG. 3.— CARMA CO($J = 3 \rightarrow 2$) line profile (solid) without continuum subtraction is over-plotted on the continuum-subtracted PdBI CO($J = 2 \rightarrow 1$) line profile (dashed). The velocity scale is with respect to $z = 0.6537$, which corresponds to the dynamical center of the CO($J = 2 \rightarrow 1$) line. The spectral resolution for CO($J = 3 \rightarrow 2$) and CO($J = 2 \rightarrow 1$) is 35.8 km s^{-1} and 21.5 km s^{-1}, respectively.

cal Satellite (*IRAS*; Neugebauer et al. 1984), and the Multiband Imaging Photometer (MIPS; Rieke et al. 2004) and Mid-infrared Infrared Array Camera (IRAC; Fazio et al. 2004) on the *Spitzer Space Telescope*. We retrieve PBCD (level 2) *Spitzer*/IRAC images from the Spitzer Heritage Archive and perform aperture photometry on the channel 1 image to extract the flux density at 3.6 μm since it is not available from the IRSA archive.

The emission in the IRAC images is slightly extended. We thus use the *HST* image ($\sim 0.''07$ resolution) to determine origins of their centroids, all of which are found to be centered at the position corresponding to the lensed emission from the background galaxy. To recover the diffuse background emission, we subtract a point source model centered on the lensing galaxy, using the average FWHM found by fitting a Gaussian profile to several field stars with the IMEXAM routine of IRAF. We perform aperture photometry on the residual image to obtain decomposed flux measurements from the background galaxy. The photometry for the foreground galaxy is then obtained by subtracting the background emission from the observed total flux. The resulting photometry in Table 1 are obtained after performing an aperture correction described in the IRAC Instrument Handbook[3] to correct for the fact that the imaging was calibrated using a 12$''$ aperture, which is larger than the aperture (5.''8) we used to perform aperture photometry.

We fit a power-law spectrum to the decomposed IRAC photometry to disentangle the background and foreground emission from the total flux observed in the MIPS 24 μm band. The spectral indices corresponding to best-fitting curves are $\alpha = -1.8$ and $\alpha = -0.85$ for the lensing galaxy and RXJ1131, respectively. The latter is consistent with the mean 3.6−8 μm spectral slope of $\alpha = -1.07 \pm 0.53$ found for unobscured AGN (Stern et al. 2005). An extrapolation of the fit to 24 μm yields 33.96 ± 0.01 mJy and 25.19 ± 0.03 mJy for the foreground galaxy and RXJ1131, respectively. The uncertainties are the standard deviations of the extrapolated fluxes obtained from two independent Monte Carlo simulations, each of 500 iterations.

[3] http://irsa.ipac.caltech.edu/data/SPITZER/docs/irac/iracinstrumenthandbook/
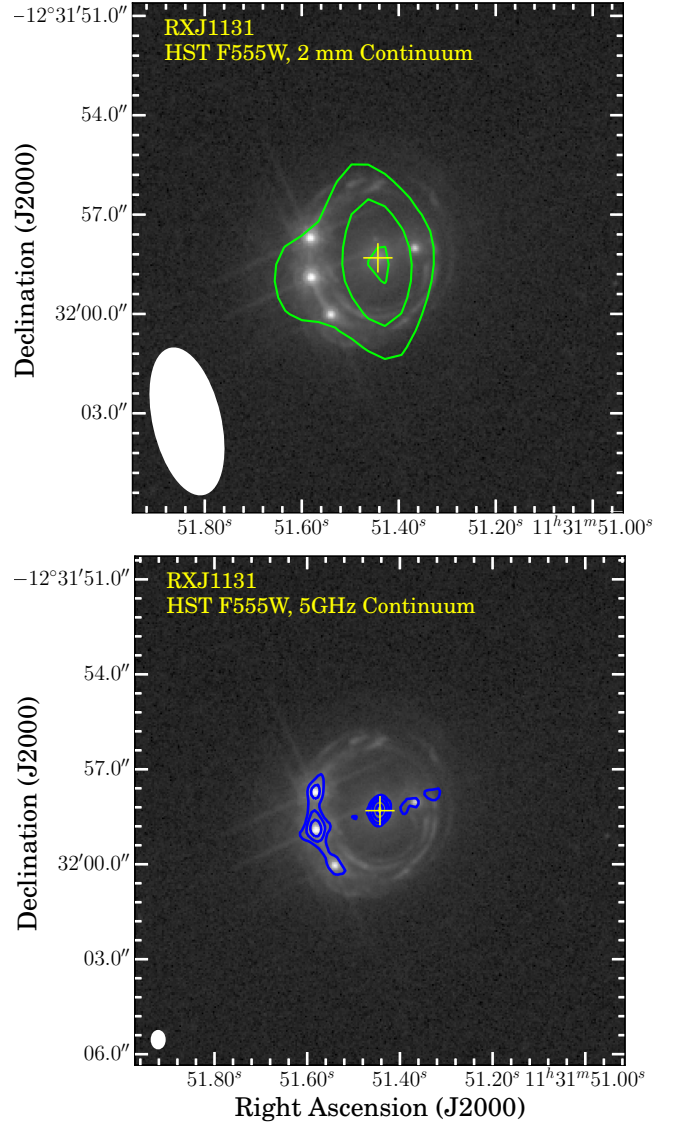

FIG. 4.— Top: overlay of the 2 mm continuum emission on the optical image. Bottom: overlap of the VLA 5 GHz continuum emission on the optical image. Contours in both images start and increment at steps of $\pm 3\sigma$, where $\sigma_{2mm} = 0.082$ mJy beam^{-1} and $\sigma_{5GHz} = 13$ μJy beam^{-1} in the top and bottom panel, respectively. The central crosses indicate the centroid of the foreground galaxy, as detected in the optical image. The synthesis beam size is $4.''4 \times 2.''0$, at PA = 13° for the PdBI observations (top), and $0.''5 \times 0.''4$ (PA = 0.18°) for the VLA observations (bottom).

We incorporate the decomposed 24 μm data in our SED fitting to provide some constraints on the Wien tail beyond the dust peak of the spectral energy distribution (SED) of RXJ1131. Details of the SED modeling are presented in §5.4.

Extraction of the *Herschel*/SPIRE photometry at 250, 350, and 500 μm was carried out using SUSSEXTRACTOR within the Herschel Interactive Processing Environment (HIPE; Ott 2010) on Level 2 maps obtained from the Herschel Science Archive. These maps were processed by the SPIRE pipeline version 13.0 within HIPE. The SUSSEXTRACTOR task estimates the flux density from an image convolved with a kernel derived from the SPIRE beam. The flux density measured by SUSSEXTRACTOR is addi-

TABLE 1
PHOTOMETRY DATA

Wavelength μm	Frequency GHz	Flux Density mJy	Instrument
		Combined/Unresolved	
1.25	239834	1.009 ± 0.09	2MASS/J-Band
1.65	181692	1.448 ± 0.12	2MASS/H-Band
2.17	138153	2.064 ± 0.16	2MASS/Ks-Band
3.4	88174.2	7.027 ± 0.14	*WISE*/W1
3.6	83275.7	5.618 ± 0.0021	*Spitzer*/IRAC
4.5	66620.5	7.803 ± 0.0021	*Spitzer*/IRAC
4.6	65172.3	8.872 ± 0.16	*WISE*/W2
5.8	51688.4	10.720 ± 0.0051	*Spitzer*/IRAC
8.0	37474.1	14.470 ± 0.0041	*Spitzer*/IRAC
12	24982.7	21.960 ± 0.42	*WISE*/W3
12	24982.7	<400	*IRAS*
22	13626.9	55.110 ± 1.9	*WISE*/W4
24	12491.4	70.204 ± 0.026	*Spitzer*/MIPS
25	11991.7	< 500	*IRAS*
60	4996.54	< 600	*IRAS*
100	2997.92	< 1000	*IRAS*
250	1199.17	289.4 ± 9.6	*Herschel*/SPIRE
350	856.55	168.2 ± 8.6	*Herschel*/SPIRE
500	599.585	56.8 ± 8.8	*Herschel*/SPIRE
1387.93	216	<2.492	CARMA
2152.82	139.256	1.230 ± 0.220	PdBI
		Foreground Lensing Galaxy	
0.555	540167	0.056 ± 0.006	*HST*-ACS/V-Band
0.814	368295	0.238 ± 0.013	*HST*-ACS/I-Band
1.6	187370	0.539 ± 0.041	*HST*-NICMOS(NIC2)/H-Band
3.6	83275.7	0.585 ± 0.003 [a]	*Spitzer*/IRAC
4.5	66620.5	1.794 ± 0.0027 [a]	*Spitzer*/IRAC
5.8	51688.4	3.163 ± 0.0059 [a]	*Spitzer*/IRAC
8.0	37474.1	4.589 ± 0.0057 [a]	*Spitzer*/IRAC
2152.82	139.256	0.799 ± 0.082	PdBI
61414	4.8815	0.866 ± 0.027	VLA
		Background Galaxy RXJ1131	
0.555	540167	0.009 ± 0.0041	*HST*-ACS/V-Band
0.814	368295	0.041 ± 0.0054	*HST*-ACS/I-Band
1.6	187370	0.133 ± 0.004	*HST*-NICMOS(NIC2)/H-Band
3.6	83275.7	5.034 ± 0.0021	*Spitzer*/IRAC
4.5	66620.5	6.009 ± 0.0017	*Spitzer*/IRAC
5.8	51688.4	7.557 ± 0.003	*Spitzer*/IRAC
8.0	37474.1	9.881 ± 0.0039	*Spitzer*/IRAC
2152.82	139.256	0.400 ± 0.082 [b]	PdBI
61414	4.8815	1.273 ± 0.042	VLA

REFERENCES. — The *HST* photometry is taken from C06.

NOTE. — The IRAC photometry for channel 1 (3.6 μm) is extracted directly from the image and from the Spitzer Heritage Archive for channels 2–4 (4.5, 5.8, and 8.0 μm). All upper limits are 3σ.
[a] Flux obtained using aperture photometry after subtracting the emission of RXJ1131 from the total emission.
[b] Flux extracted from the residual map after subtracting a point-source model.

tionally confirmed using the Timeline Fitter, which performs photometry by fitting a 2D elliptical Gaussian to the Level 1 data at the source position given by the output of SUSSEXTRACTOR. The fluxes obtained from both methods are consistent within the uncertainties.

5. ANALYSIS

5.1. *Lens Modeling*

At the angular resolution of the CO($J = 2 \to 1$) data, the images are resolved over $\sim$2 resolution elements. Given the extent of the lensed emission (see Figure 2), this implies that we do not resolve structures (e.g. knots and arcs) of the lensed emission in our CO($J = 2 \to 1$) data. Never-

theless, the high spectral resolution of these data provides dynamical information on spatial scales smaller than the beam (see Figure 2). Hence, we reconstruct the intrinsic gas dynamics by carrying out a parametric lens modeling over different channel slices of the interferometric data using our lensing code UVMCMCFIT (Bussmann et al. 2015a; see Bussmann et al. 2015b for details of the code). Models of each slice thus provide information on the corresponding kinematic component of the CO gas, enabling us to reconstruct the source plane velocity gradient. In order to have adequate SNRs for lens modeling, we bin the frequency channels by a factor of five to produce seven independent $\Delta v \sim 105\,\mathrm{km\,s^{-1}}$ channels (dashed line in Figure 5) that cover the full linewidth of $\sim$750 km s^{-1}.
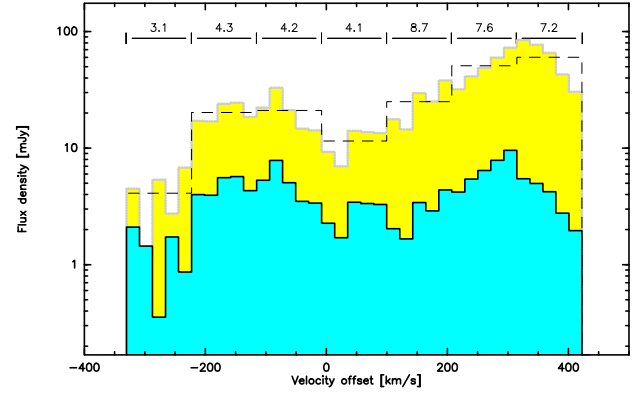

FIG. 5.— The full resolution CO($J = 2 \to 1$) spectrum (yellow histogram) and the binned spectrum (dashed line) with the seven $\Delta v \sim 105\,\mathrm{km\,s^{-1}}$ channels used for lens modeling. The blue histogram shows the "intrinsic" line profile of RXJ1131 after subtracting a contribution from its companion galaxy and correcting for lensing using the magnification factors μ_L as annotated by the horizontal bars shown above the respective model channels. Flux density on the y-axis is shown on a log scale.

The lens mass distribution is modeled using a singular isothermal ellipsoid (SIE) profile, which is described by five free parameters: the positional offset in R.A. and Dec. relative to an arbitrary chosen fixed coordinate in the image, the Einstein radius, the axial ratio, and the position angle. We use the VLA radio continuum emission toward the foreground galaxy to initialize the positional offset. We impose a uniform prior $\pm 0\rlap{.}''05$ in both ΔR.A. and ΔDec., motivated by the astrometry uncertainties in the VLA image as well as the uncertainties provided by previous SIE lens model (C06). We initialize the Einstein radius based on the model parameters reported by C06 and impose a uniform prior using $\pm 3\sigma$ of their uncertainties. The sources are modeled using elliptical Gaussian profiles, which are parameterized by six free parameters: the positional offset in R.A. and Dec. relative to the lens, the intrinsic flux density, the effective radius, the axial ratio, and the position angle. The position of each source is allowed to vary between $\pm 1\rlap{.}''5$ (i.e., within the Einstein radius) and the effective radius is allowed to vary from $0\rlap{.}''01$–$2''$.

Our code uses an Markov Chain Monte Carlo (MCMC) approach to sample the posterior probability distribution function (PDF). In each model, we require a target acceptance rate of $\sim$0.25−0.5 and check for chain convergence by inspecting trace plots and by requiring the samples are

TABLE 2
LENS PARAMETERS CONSTRAINED BY
MODELS OF SEVEN VELOCITY CHANNELS

Parameters		Median values
Offset in RA	($''$)	0.004 ± 0.027
Offset in Dec	($''$)	0.003 ± 0.027
Axial Ratio		0.56 ± 0.16
Position Angle	(deg)	103 ± 22
Einstein Radius	($''$)	1.833 ± 0.002

NOTE. — Parameters describing the foreground lens are obtained based on the median in the preliminary models (see text for details). All angular offsets are with respect to $\alpha = 11^{\rm h}31^{\rm m}51\overset{s}{.}44$, $\delta = -12°31'58\overset{''}{.}3$ (J2000).

obtained beyond at least an autocorrelation time. We thus employ ∼50,000 samples as the initial "burn-in" phase to stabilize the Markov chains (which we then discard) and use the final ∼5,000 steps, sampled by 128 walkers, to identify the posterior. Here, we identify the best-fit model and the quoted uncertainties using the median and the 68% confidence intervals in the marginal PDFs.

We first obtain a preliminary lens model for each channel slice independently, where their lens parameters are allowed to vary and are initialized according to the aforementioned way. We obtain the final model by repeating the modeling over each slice but fixing their lens parameters to the overall median in the preliminary models, as listed in Table 2. This ensures that all models share the same lens profile. The magnification factors in Table 3 are determined by taking the ratio between the image plane flux and the source plane flux of each model.

Our model parameters in Table 2, describing the mass distribution of the lensing galaxy, are consistent (within the uncertainties) with that of the SIE model presented by C06. We find a mass of $M(\theta < \theta_{\rm E}) = (7.47 \pm 0.02) \times 10^{11} \, M_\odot$ within the Einstein radius.

5.1.1. *Interpretation of the Source-plane Morphology*

The reconstructed source locations in Figure 6 demonstrate an intrinsic velocity gradient across the source plane, which is consistent with a kinematically-ordered disk-like galaxy. Additional support to the disk conjecture can be found in the double-horned line profile (Figure 1) and the observed (image plane) velocity field (Figure 2). Furthermore, C06 also find that the reconstructed source plane emission in optical-NIR is best-reproduced using a $n = 1$ Sersic profile. We thus interpret RXJ1131 as a disk galaxy.

A better fit is found for the lens model of the red-most channel if we add a second source component (see top left panel in Figure 6). This is consistent with previous results reported by Brewer & Lewis (2008, hereafter B08), who find an optically faint companion (component F in their paper) ∼2.4 kpc in projection from the AGN host galaxy in V-band, and with C06, who find evidence for an interacting galaxy near RXJ1131. Spatially, the red velocity component of the CO emission also coincides with this component F. It is therefore likely that we detect $CO(J = 2 \rightarrow 1)$ emission in a companion galaxy.

The type of merger (major v.s. minor) in a pair of in-

teracting galaxies is most commonly distinguished based on the ratio between their total galaxy mass. Here, we use the gas mass ratio between RXJ1131 and its companion galaxy instead, given that we do not have stringent constraints on their individual galaxy mass. We decompose the total line flux into two components: one from RXJ1131 and the other from its companion. Since the companion is only detected in the red-most channel, we derive its intrinsic gas mass using the best-fit flux densities and magnification factors obtained from the models of this channel. Assuming a brightness temperature ratio of $r_{21} = 1$ between $CO(J = 2 \rightarrow 1)$ and $CO(J = 1 \rightarrow 0)$ lines and a CO luminosity-to-H$_2$ mass conversion factor of $\alpha_{\rm CO} = 0.8 \, M_\odot \, ({\rm K \, km \, pc^2})^{-1}$, we find a molecular gas mass of $M_{\rm gas} = (1.92 \pm 0.09) \times 10^9 \, M_\odot$. For the molecular gas mass in RXJ1131, we derive its intrinsic line flux over the FWZI linewidth using the respective magnification factors listed in Table 3, which to first order takes into account effect of differential lensing. This yields $I_{CO(J = 2 \rightarrow 1)} = 2.93 \pm 0.70$ Jy km s^{-1}, where the uncertainty includes those on the magnification factors. Adopting the same brightness temperature ratio and $\alpha_{\rm CO}$ as used for the companion, this corresponds to a gas mass of $M_{\rm gas} = (1.38 \pm 0.33) \times 10^{10} \, M_\odot$, which implies a *gas* mass ratio of ∼7:1 between RXJ1131 and its companion. We thus classify the system to be a *"wet-wet" minor merger*. We caution that this is based on their gas mass ratio rather than their total galaxy mass ratio, which is more commonly used in literature as the classification scheme to separate major mergers from minor mergers.

The spatial resolution of the data in hand is a few arcsec, which implies that despite the high SNR and spectral resolution, constraints on the intrinsic sizes of the lensed galaxies are modest, and thus the magnification factors may be under-predicted.

5.1.2. *Spatial Extent and Differential Lensing*

In the image plane shown in Figure 2, the redshifted component is cospatial with the Einstein ring seen in the optical image, with most of its apparent flux originating from the lensed arc in the southeast, whereas the blue component is predominately coming from solely the lensed arc. To further illustrate this, we show the channel maps of 21.5 km s^{-1} width and a spatial spectra map of $1\overset{''}{.}5$ resolution in Figure 7 and Figure 8, respectively. The figures show that emission is present to the west, peaking toward the lensing arc (black crosses in Figure 7) in the red wing, and shifts to the east with decreasing velocity (blue wing). This is consistent with the source plane positions in our models and is suggestive of an extended CO emitting region.

Similar to previous studies of RXJ1131, where differential lensing across *HST V*-, *I*-, and *H*-band has been detected with a magnification factor decreasing from 10.9 to 7.8 (C06), the highly asymmetric $CO(J = 2 \rightarrow 1)$ line profile suggests that differential lensing is also non-negligible for CO, causing the redshifted emission to be apparently much brighter than the blueshifted component and the asymmetric line profile. This can be explained by the
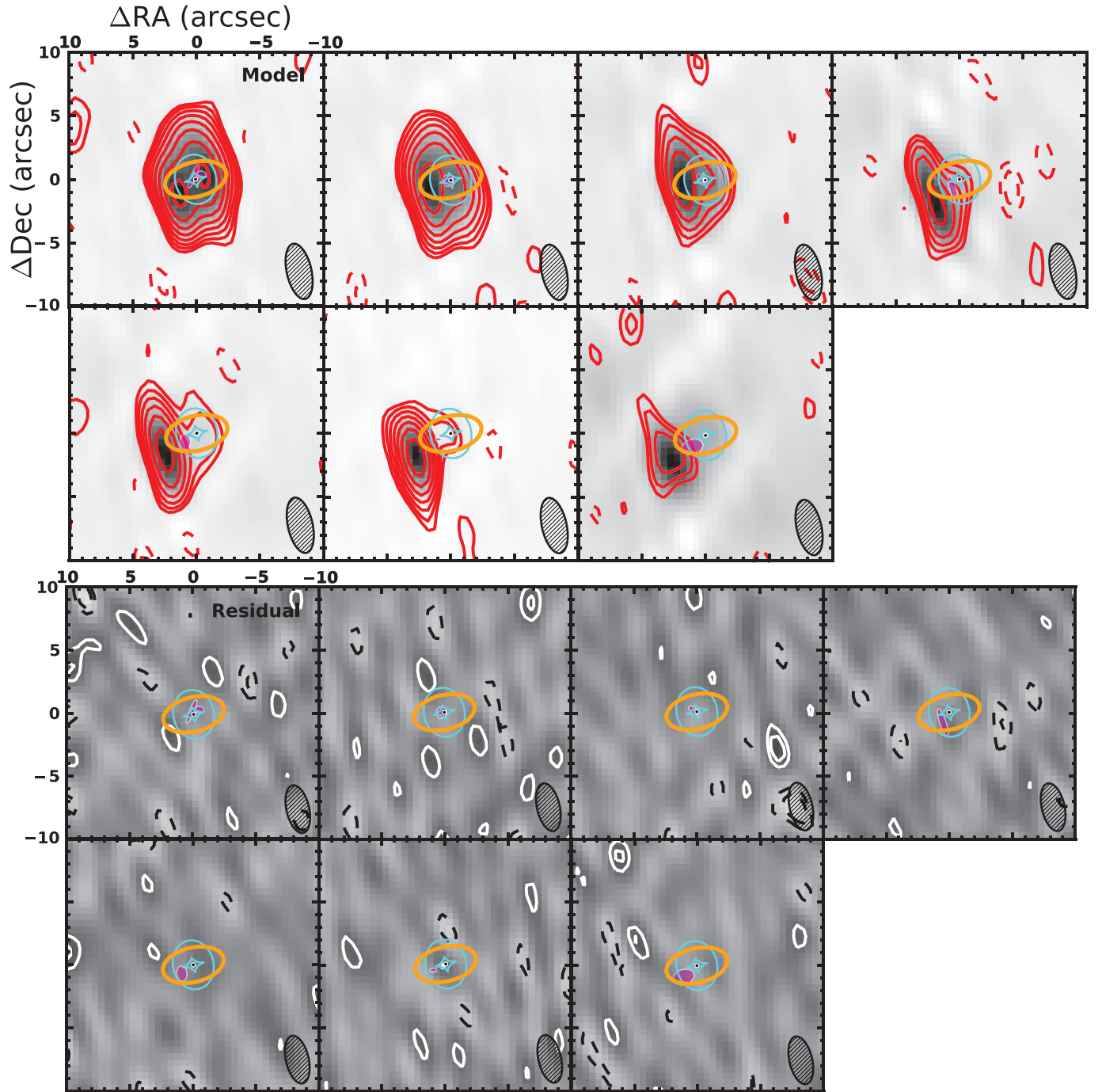
FIG. 6.— Each panel corresponds to a lens model of RXJ1131 performed over a channel slice $\sim100\,\mathrm{km\,s^{-1}}$ of the CO($J=2\rightarrow1$) data. Top: channel maps of the PdBI CO($J=2\rightarrow1$) emission (red) overlaid on our best-fit lens models (grayscale). The location of the foreground lensing galaxy is indicated by a black dot and its critical curve is traced by the orange solid line. The locations and morphologies (half-light radii) of the reconstructed sources are represented by magenta ellipses. The caustic curves are represented as cyan lines. The beam of the PdBI observations is shown in the bottom right corner of each panel. Bottom: residual images of the best-fit models, obtained by taking the Fourier transform after subtracting the best-fit model from the data in the uv-domain. Contours start at $\pm3\sigma$ and increment at steps of $3\times2^n\sigma$, where n is a positive integer.
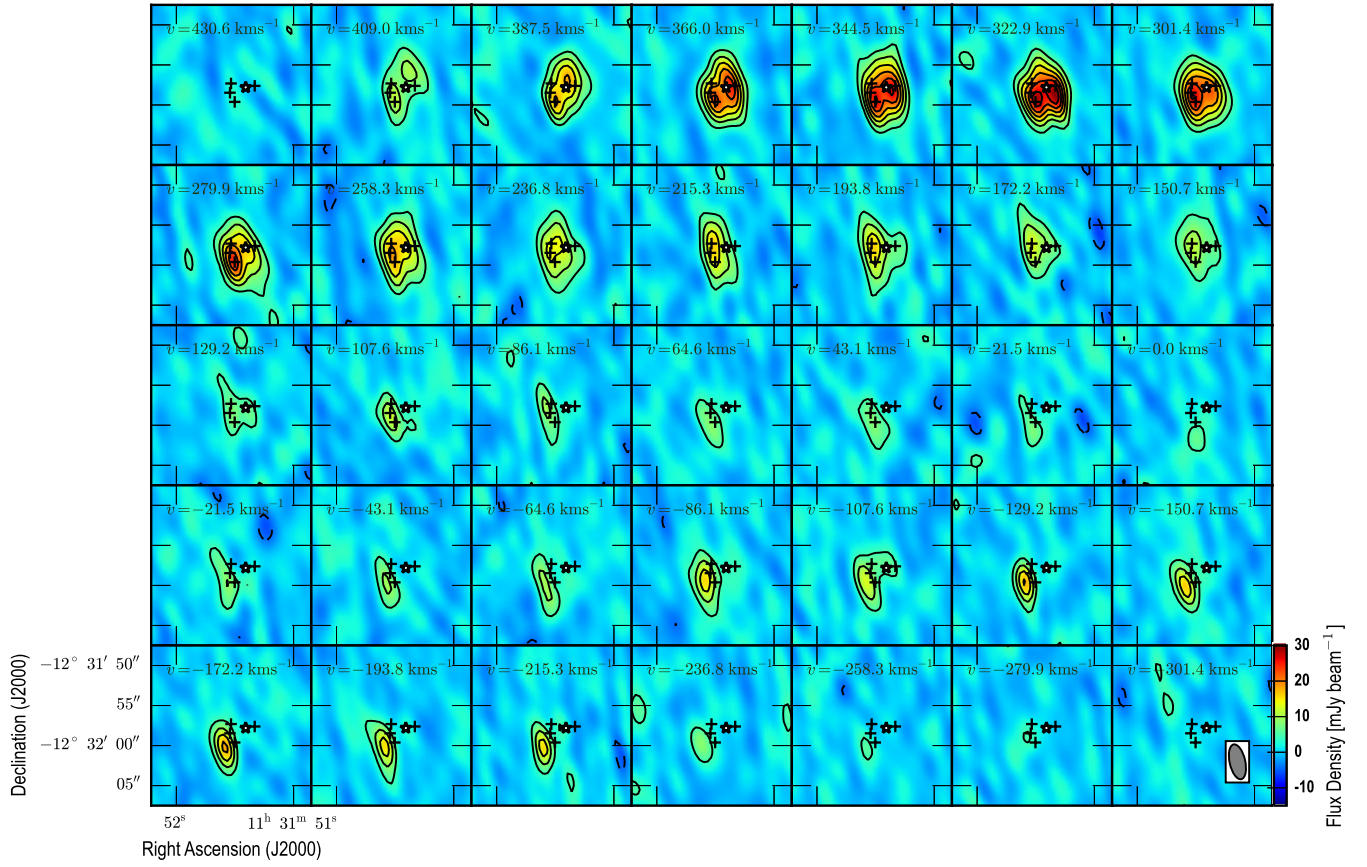
FIG. 7.— Channel maps of the PdBI CO($J = 2 \rightarrow 1$) data cube toward RXJ1131 at 21.5 km s^{-1} resolution. Black crosses indicate the positions of the lensed knots (AGN emission, which correspond to components ABCD in C06). The central white-filled star indicates the position of the foreground lensing galaxy (component G in C06). Central velocities are shown at the top of each map. Contours start and increment at steps of $\pm 3\sigma$. The beam is denoted in the bottom right panel.
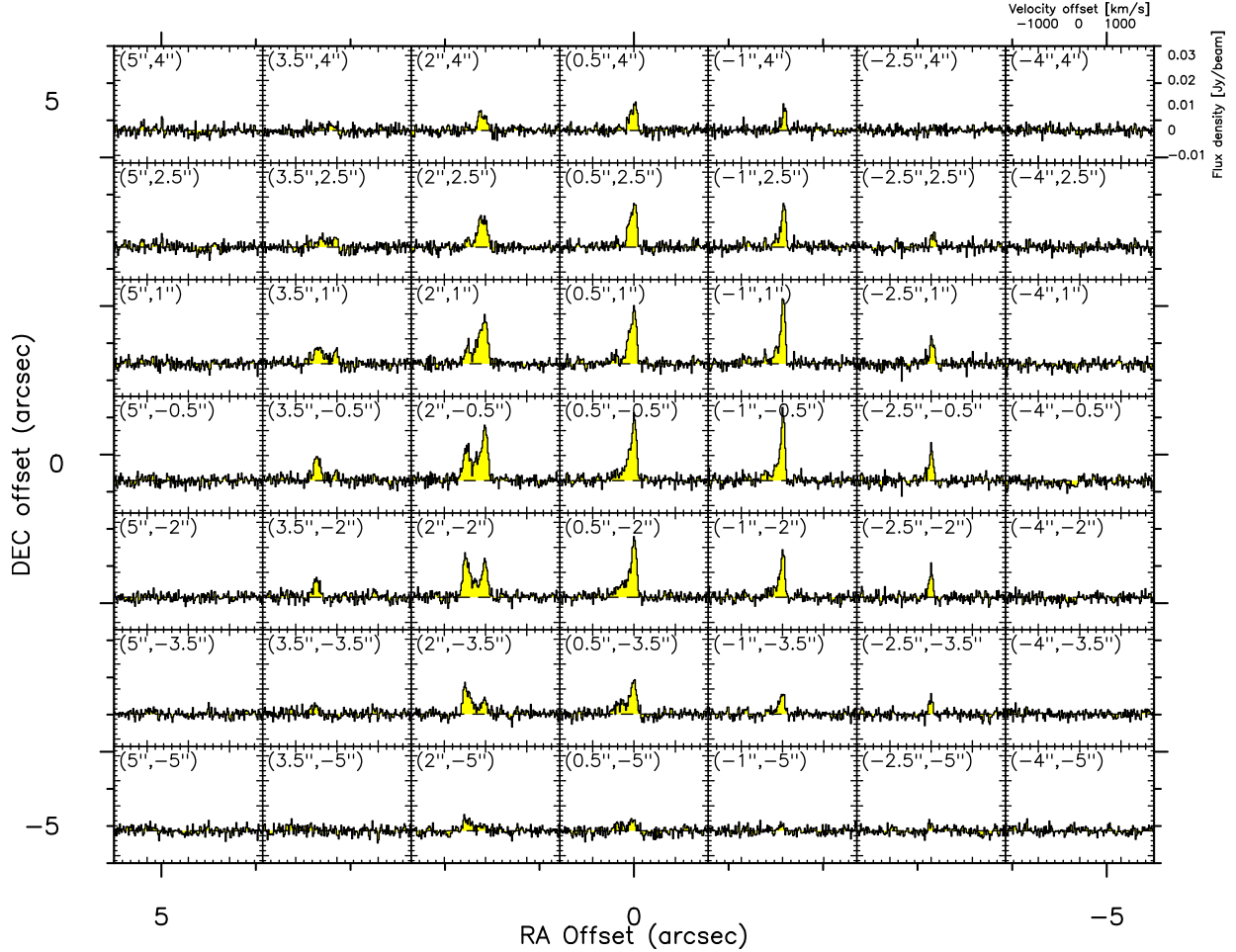
FIG. 8.— CO($J = 2 \rightarrow 1$) spectrum as a function of position, binned by 3 pixels in each direction (1.″5). The spectra map covers an extent of ∼10"×10" centered on the pixel that corresponds to the lensing galaxy. Spatial offset in arcsec is denoted in top left corner of each panel. The velocity and flux density scales are denoted in the top right panel.

TABLE 3
MAGNIFICATION FACTORS OF VARIOUS KINEMATIC
COMPONENTS IN CO($J = 2 \rightarrow 1$)

Velocity Range (km s^{-1})	Source 1 μ_L	Source 2 μ_L
-366 − -258	3.1 ± 0.9	
-237 − -151	4.3 ± 2.4	
-129 − -43	4.2 ± 0.6	
-21.5 − 65	4.1 ± 0.9	
86 − 172	8.7 ± 2.0	
194 − 280	7.6 ± 1.6	
301 − 388	7.2 ± 5.6	6.7 ± 2.5
weighted average	4.4	
median	5.5	

NOTE. — Velocity is taken from the center of each (native) channel without any binning. Each row corresponds to a channel slice used for lens modeling. Source 1 is RXJ1131 and source 2 is its companion. See text for details.

difference in magnification factor (μ_L) which varies from 8.7 to 3.1 across the CO($J = 2 \rightarrow 1$) line (Table 3) and also partly due to a contribution from the companion in the redshifted velocity channels. The variation in μ_L across channels is consistent with the source plane positions relative to the caustics in Figure 6, where the red wing emission mainly originates near the cusp of the caustic and the blue

wing emission is located beyond the caustics. In fact, the intrinsic line flux of the redshifted and blueshifted emission in RXJ1131 (after subtracting a contribution from the companion) is $I_{CO(J = 2 \rightarrow 1)} = 1.26 \pm 0.23$ Jy km s^{-1} and 1.25 ± 0.23 Jy km s^{-1}, respectively, implying an intrinsically symmetric line profile (Figure 5). This is consistent with the source-plane velocity gradient in our lens model (Figure 6 and Figure 9).

5.2. *CO($J = 2 \rightarrow 1$) Kinematics*

Fitting a four-parameter double-Gaussian that describes two velocity peaks by a single FWHM to the "intrinsic" CO($J = 2 \rightarrow 1$) line profile of RXJ1131 (after correcting for lensing using the magnification factors for various channels and separating the emission from RXJ1131 and its companion), we find a roughly symmetric double-horned profile with a flux ratio of 1.2 ± 0.4 between the peaks, which are separated by $\Delta v_{sep} = 387 \pm 45$ km s^{-1}, and a FWHM of 220 ± 72 km s^{-1}. The peak separation obtained from this "intrinsic" line profile is slightly lower than that obtained from the observed spectrum (i.e., without lensing corrections). This discrepancy is likely a result of differential lensing, which causes the line peak of the red wing to shift towards higher velocity chan-

nels, biasing the centroid of one of the components in a double-Gaussian to higher velocity than otherwise. If we instead fit with a single-Gaussian, we find a FWHM of $600 \pm 160\,\mathrm{km\,s^{-1}}$ for RXJ1131 and $73 \pm 43\,\mathrm{km\,s^{-1}}$ for the companion galaxy.

A clear velocity gradient and a high velocity dispersion ($\gtrsim 400\,\mathrm{km\,s^{-1}}$) near the central region is seen in Figure 2. While beam smearing is inevitably the dominant factor in the observed velocity dispersion at the spatial resolution of these data, the exceedingly high velocity dispersion may hint at potential perturbations from the AGN, or internal turbulence due to interactions with the companion, and/or instability due to the large gas content. Therefore, in this scenario, RXJ1131 is consistent with a disrupted disk galaxy hosting an optically bright quasar and is in the process of merging.

5.3. *CO(J = 2 → 1) Dynamical Modeling*

Assuming the velocities of the respective channels used in the lens modeling correspond to solely the tangential component of the true velocity vector of a rotating disk (i.e., along the major axis), we extract a one dimensional PV diagram in Figure 9 by slicing across their source plane positions (PA: 121°).

We then attempt to characterize the molecular gas kinematics using an empirically-motivated disk model (e.g., Courteau 1997; Puech et al. 2008; Miller et al. 2011):

$$V = V_0 + \frac{2}{\pi} V_a \arctan\left(\frac{R}{R_t}\right), \qquad (1)$$

where V is the observed velocity, V_0 is the velocity at dynamical center, V_a is the asymptotic velocity, and R_t is the "turnover" radius at which the rising part of the curve begins to flatten. We perform non-linear least square fitting using an orthogonal distance regression to find the best-fit parameters, taking into account the uncertainties in both velocity (channel width) and distance offset. We also place an upper limit on $R_t < 15$ kpc to keep this parameter physical (e.g., Puech et al. 2008; Miller et al. 2011). The parameter uncertainties are inferred based on a Monte Carlo simulation of 500 iterations, where the input parameters are perturbed according to random Gaussian distributions of sigmas corresponding to their uncertainties. Using this model, we find $V_a = 975 \pm 387\,\mathrm{km\,s^{-1}}$, $R_t = 10.7 \pm 5.7$ kpc, and $V_0 = 28 \pm 40\,\mathrm{km\,s^{-1}}$. However, since emission is not resolved along the flat regime of the rotation curve, the asymptotic velocity and the "turnover" radius are poorly constrained. In particular, V_a and R_t are highly correlated with a Pearson coefficient $R = 0.998$, and 0.027 between V_a and V_0.

The asymptotic velocity (V_a) – an extrapolation of the model out to radius beyond the disk scale-length and half-light radius – is not equivalent to maximum observed velocity ($V_{\max}$), which is commonly used in literature to parameterize disk rotation. The arctangent model is most commonly used in studies of the Tully-Fisher relation, where an extrapolation to $V_{2.2}$ (velocity at 2.2 disk scale-

length or $\sim$1.375 half-light radius, or $\sim 0.7 R_{\mathrm{opt}}$[4]) is typically adopted as the rotation velocity ($V_{\max}$ in their terminology) since this corresponds to the radius at which the velocity of a pure exponential disk peaks (Courteau & Rix 1997). Here, we adopt the maximum *observed* velocity $V_{\mathrm{rot}} = 345 \pm 55\,\mathrm{km\,s^{-1}}$ at 6 ± 3 kpc from the dynamical center as a proxy to the rotation velocity. This radius corresponds to $\sim 0.6\,R_e$, where R_e is the half-light radius $\sim$10.3 kpc inferred from the *HST I*-band lens model (C06; converted to our cosmology). We note that the source plane half-light radius varies substantially with wavelength. In particular, the half-light radius is found to be ~ 4 kpc and ~ 7 kpc in *V*-band (B08) and *H*-band (C06), respectively. The CO gas is thus of similar spatial extent as in *H* and *I*-bands.

In the rest-frame, emission in the observed-frame *H*-band corresponds to NIR emission ($\sim 1\,\mu$m), tracing radiation from the accretion disk surrounding the central AGN and also from old and evolved stellar populations; *I*-band corresponds to roughly the optical *V*-band, tracing stellar radiation from existing, less massive (i.e., longer-lasting) stars; *V*-band corresponds to roughly *U*-band, tracing radiation from massive young stars in the host galaxy. Hence, the *V*-band compactness may be explained in part due to the fact that its emission is more susceptible to dust extinction than in other bands and/or a central starburst caused by higher concentrations of star-forming gas towards the central regions – owing to gravitational perturbations induced from interactions with the companion (e.g., Di Matteo et al. 2005). This is consistent with the picture that old stars form first and constitute the bulge component of a spiral galaxy and that nuclear starbursts (in the inner few kpc) can be triggered at a later time as the progenitor disk galaxy interacts with other galaxies to form a larger bulge.

5.4. *SED Modeling*

We fit dust SED models to the $24\,\mu$m–2.2 mm photometry in Figure 10, where we also include the IRAS $60\,\mu$m and $100\,\mu$m upper limits to constrain the dust peak. The fit is performed with the code MBB_EMCEE (e.g., Riechers et al. 2013; Dowell et al. 2014), which samples the posterior distributions using an MCMC approach and uses instrumental response curves to perform color correction on-the-fly. The SED model consists of a modified-blackbody function with a power-law attached to the Wien side to account for an excess in the MIR owing to emission of warm and small dust grains. The model is thus described by five free parameters: the rest-frame characteristic dust temperature (T_d), the emissivity index (β), the power-law index (α), the flux normalization at $500\,\mu$m (f_{norm}), and the observed-frame wavelength at which the emission becomes optically thick (λ_0). We impose a uniform prior with an upper limit of 100 K on T_d (see e.g., Sajina et al. 2012), a Gaussian prior centered around $\mu = 1.9$ with $\sigma = 0.3$ on β, and a uniform prior with an upper limit of $1000\,\mu$m on λ_0. We check for chain convergence by requiring that the autocorrelation length of each parameter
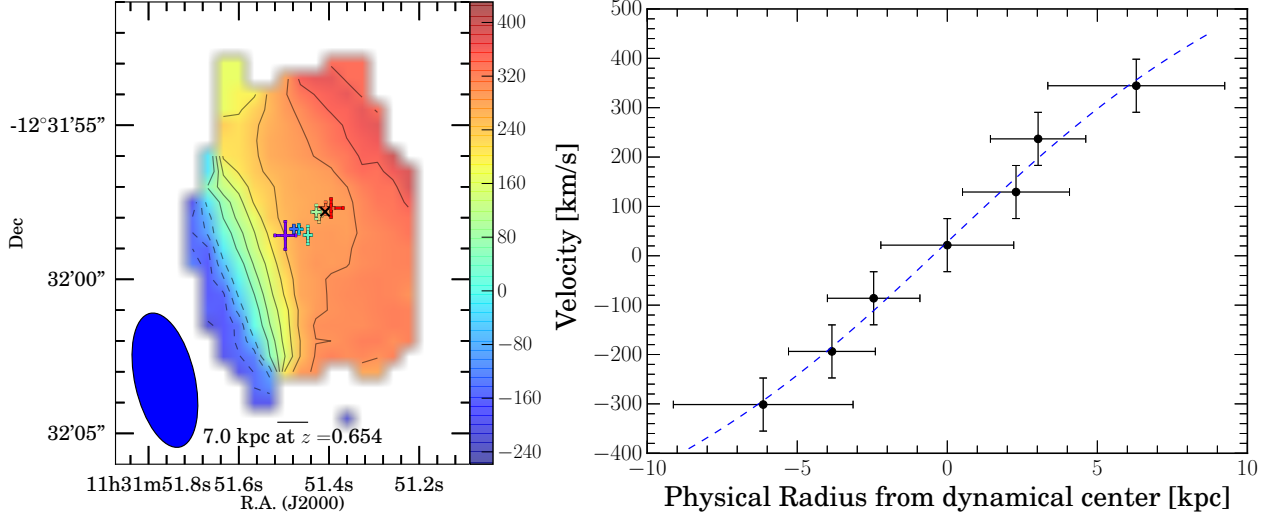
---

[4] Radius enclosing 83% of the light distribution.

FIG. 9.— Left: Source-plane positions from best-fit CO($J = 2 \to 1$) lens models are indicated with their associated uncertainties atop the observed first moment map. The contours are at steps of 50 km s^{-1}. Right: PV slice along the major axis in the source plane at PA = 121°. Dashed line shows the best-fit rotation curve using an arctangent model. The vertical error bars show the channel width for each model and the horizontal error bars are the 1σ uncertainties on the source plane positions.

TABLE 4
SED FITTING RESULTS

Parameters		With 24μm	Without 24μm
T_d	(K)	$52.0^{+4.0}_{-4.1}$	$58.2^{+14.5}_{-14.4}$
β		$1.8^{+0.5}_{-0.6}$	$2.1^{+0.3}_{-0.3}$
α		$1.6^{+0.5}_{-0.5}$	$8.9^{+6.9}_{-6.3}$
λ_0 [a]	(μm)	548^{+285}_{-307}	367^{+125}_{-145}
λ_{peak} [b]	(μm)	162^{+16}_{-30}	146^{+39}_{-44}
$f_{norm,\,500\mu m}$ [c]	(mJy)	59^{+14}_{-13}	60^{+5}_{-5}
L_{FIR} [d]	($10^{12}\,L_\odot$)	$3.81^{+2.04}_{-1.92}$	$4.72^{+2.54}_{-2.26}$
M_d [e]	($10^8\,M_\odot$)	22^{+5}_{-18}	11^{+5}_{-6}

NOTE. — Errors reported here are $\pm 1\sigma$. L_{FIR} and M_d are not corrected for lensing.

[a] Observed-frame wavelength where $\tau_\nu = 1$
[b] Observed-frame wavelength of the SED peak
[c] Observed-frame flux density at 500 μm
[d] Rest-frame 42.5–122.5 μm luminosity
[e] Derived assuming absorption mass coefficient of $\kappa = 2.64\,\mathrm{m^2\,kg^{-1}}$ at $\lambda = 125.0\,\mu$m (Dunne et al. 2003)

is less than the number of steps taken for the burn-in phase (which are then discarded). Here we report the statistical means and the 1σ confidence interval in the marginal PDFs as the best-fit parameters, as listed in Table 4.

In the first model, we include the 24 μm data to constrain the power-law index. Based on the best-fit of this model, we find an apparent far-IR luminosity (rest-frame 42.5 – 122.5 μm) of $3.81^{+2.04}_{-1.92} \times 10^{12}\,L_\odot$ and a dust mass of $22^{+5}_{-18} \times 10^8\,M_\odot$, uncorrected for lensing. For the mass absorption coefficient, we adopt $\kappa = 2.64\,\mathrm{m^2 kg^{-1}}$ at rest-frame 125.0 μm (Dunne et al. 2003). The dust mass uncertainty does not include that of the absorption coefficient.

A fit including the MIR 24 μm photometry is likely an upper limit on the far-IR luminosity due solely to star formation in the AGN host galaxy. If we instead fit for a model excluding this constraint, two major consequences are immediately apparent. First, the power-law index is

poorly-constrained (see Table 4). Second, the steep power-law implies only a small contribution from the power-law regime to the total IR luminosity as compared to the graybody component. Thus, the far-IR luminosity in this model should, in principle, correspond to a lower limit on the cold dust emission. Using the best-fit parameters for this model, we find a total IR luminosity L_{IR} (rest-frame $8 - 1000\,\mu$m) of $9.71^{+6.14}_{-6.05} \times 10^{12}\,L_\odot$, a far-IR luminosity L_{FIR} of $4.72^{+2.54}_{-2.26} \times 10^{12}\,L_\odot$ and a dust mass M_{dust} of $11^{+5}_{-6} \times 10^8\,M_\odot$, all of which are uncorrected for lensing. Taken at face value, this implies a FIR-to-IR luminosity ratio of $\sim 58 \pm 35\%$.

The dust temperature from both models is similar to that of ULIRGs at $0.6 < z < 1.0$ (54 ± 5 K; Combes et al. 2013, hereafter C13). We note the far-IR luminosity is comparable in both models, which is not surprising given the lack of constraints in the MIR. For the subsequent analysis, we adopt the physical quantities from the first model (i.e., with constraints at 24 μm). The choice of SED model does not affect the derived star formation rate (SFR) given the similar far-IR luminosity. Yet, the dust mass is higher by a factor of ~ 2 in the former but consistent within the uncertainties. We correct for lensing using the median magnification factor ($\mu_L = 5.5$) from the CO lens models. This yields a L_{FIR} of $(6.9 \pm 3.6) \times 10^{11}\,L_\odot$ and a total IR luminosity of $\sim 1.5 \times 10^{12}\,L_\odot$, implying RXJ1131 is a ULIRG. Assuming a Salpeter initial mass function (Salpeter 1955), we find a SFR$_{FIR}$ of $120 \pm 63\,M_\odot$ yr^{-1} using a standard conversion (Kennicutt 1998).

5.5. ISM Properties

In this section, we derive the gas properties of the merging system based on CO($J = 2 \to 1$) and compare them with those reported by C13 — the largest sample of ULIRGs at similar redshift ($0.6 < z < 1.0$) with CO
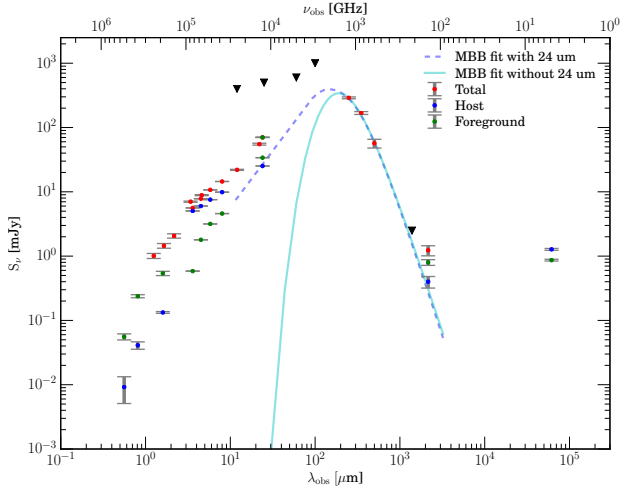
FIG. 10.— SEDs of RXJ1131 and its lensing galaxy. The photometry is listed in Table 1. Best-fit SED models of the thermal dust emission towards RXJ1131 with(out) MIR constraint at $24\,\mu m$ are plotted as dashed (solid) lines.

measurements[5]. Their results are based on unresolved CO($J = 2 \rightarrow 1$) and CO($J = 4 \rightarrow 3$) line observations with the IRAM 30-m single-dish telescope.

5.5.1. *Linewidth and Sizes*

A FWHM linewidth of $\Delta v \sim 600 \pm 160\,{\rm km\,s^{-1}}$ found for RXJ1131 by fitting a single Gaussian is considerably larger that those in the C13 sample ($370\,{\rm km\,s^{-1}}$) as well as in local ULIRGs ($300 \pm 85\,{\rm km\,s^{-1}}$, with the largest being $480\,{\rm km\,s^{-1}}$; Solomon et al. 1997, hereafter S97). Yet, given the dynamic nature of these galaxies, a CO linewidth of $\sim 600\,{\rm km\,s^{-1}}$ may not be surprising. Indeed, a linewidth of $\Delta v = 750\,{\rm km\,s^{-1}}$ has been observed in a local LIRG (Arp 118; Solomon & Vanden Bout 2005, hereafter SV05). Linewidth of this range ($\gtrsim 500\,{\rm km\,s^{-1}}$) is also commonly observed in high-z starburst galaxies (e.g., Greve et al. 2005, hereafter G05) and high-z quasar host galaxies (e.g., Coppin et al. 2008), which are believed to originate from mergers.

The CO gas in RXJ1131 is $\sim 6 \pm 3\,{\rm kpc}$ in radius (in the source plane), which is more extended than the average in a sample of disk-like U/LIRGs studied by Ueda et al. (2014), but consistent with their range of $1.1 - 9.3\,{\rm kpc}$. Our CO size is also consistent with that of high-z ($z > 1$) galaxies ($R \sim 4$–20 kpc; G05; Daddi et al. 2010; Riechers et al. 2011; Ivison et al. 2011) and local U/LIRGs in the Gao & Solomon (1999) sample ($R \lesssim 10\,{\rm kpc}$).

5.5.2. *Dynamical Mass*

Assuming the gas is virialized, the dynamical mass can be approximate as $M_{\rm dyn} = \sigma^2 R/G$, where σ is the velocity dispersion, or the rotational velocity in the case of a rotating disk model (i.e., $\sigma = V_{\rm rot} \sin i$). Using a rotational velocity $V_{\rm rot} \sin i = 345\,{\rm km\,s^{-1}}$ (see §5.3), we find

---

[5] The far-IR luminosity in C13 is derived based on $60\,\mu m$ and $100\,\mu m$ IRAS fluxes, and using a different definition of $L_{\rm FIR}$: rest-frame $40 - 500\,\mu m$. Following this convention, we find a far-IR luminosity of $L_{\rm FIR} = (8.8 \pm 0.4) \times 10^{11} (\mu_{\rm L}/5.5)^{-1}\,L_\odot$ and a SFR of $(150 \pm 70)\,M_\odot\,{\rm yr^{-1}}$ for RXJ1131.

a dynamical mass of $M_{\rm dyn} \sin^2 i\,(< 6\,{\rm kpc}) = 17 \times 10^{10}\,M_\odot$ enclosed within the CO-emitting region in RXJ1131. If we instead consider the CO($J = 2 \rightarrow 1$) line peak separation ($\Delta v_{\rm sep}/2 \sim 200\,{\rm km\,s^{-1}}$) as the rotation velocity, we find $M_{\rm dyn} \sin^2 i\,(< 6\,{\rm kpc}) = 5.8 \times 10^{10}\,M_\odot$. We derive an inclination angle of $56.4°$ from the morphological axial ratio of $a/b \sim 1{.}''8/3{.}''25$, which we estimate from the source-plane image reconstructed by C06 (Figure 3 in their paper). This corresponds to an inclination-corrected dynamical mass of $8.3 \times 10^{10}\,M_\odot < M_{\rm dyn} < 25 \times 10^{10}\,M_\odot$. Our estimate should be considered at best an upper limit since the gas in RXJ1131 is unlikely virialized. In the following sections, we use the lower limit $(8.3 \pm 1.9) \times 10^{10}\,M_\odot$ as the dynamical mass as it is derived in a manner similar to what is commonly used in literature (e.g., S97; Downes & Solomon 1998, hereafter DS98; G05).

Using the velocity dispersion obtained by fitting a single Gaussian to the line profile of the companion ($\sigma = 30\,{\rm km\,s^{-1}}$) and its intrinsic source size of $\sim 700\,{\rm pc}$ obtained from the *HST* V-band lens model (B08), we find a dynamical mass of $M_{\rm dyn} \sin^2 i = 1.5 \times 10^8\,M_\odot$. This corresponds to $M_{\rm dyn} = 5.8 \times 10^8\,M_\odot$ if we assume an inclination angle of $30°$. We adopt the V-band size as the radius R in the above estimate owing to the fact that it is the least uncertain constraint on the source size for the companion. However, since this dynamical mass is substantially lower than the gas mass, which is a more reliable estimate based on the data in hand, we do not use this dynamical mass to derive other physical parameters. The underestimated dynamical mass may reflect the dusty nature of the companion, which causes its V-band source size to appear much smaller than its true extent without any dust obscuration. If we use the half-right radius of $R_{\rm CO} = 4.2 \pm 2.8\,{\rm kpc}$ obtained from our best-fit lens model as the unobscured source size (see §5.1.1), we find a dynamical mass of $M_{\rm dyn} = (3.5 \pm 2.3) \times 10^9\,M_\odot$ (assuming $i = 30°$), which is physically more sensible than that derived using the V-band source size. The uncertainty here only includes that of the CO source size. Given the large systematic uncertainties associated with the model-based source size and the lack of constraint on the inclination angle, we do not use this dynamical mass in the remaining of this paper.

5.5.3. *Gas Mass and Gas Ratios*

Using the lensing-corrected dust mass, we find a galactic-scale gas-to-dust ratio of 40 ± 34, which is lower than the statistical average of $f_{\rm gas-dust} = 206$ in the C13 sample but well within their broad range of values over the entire sample. Our ratio is also consistent with high-z SMGs (Bothwell et al. 2013) and local ULIRGs (Wilson et al. 2008), but lower than of the Milky Way by $\sim 4\sigma$ (ignoring systematic uncertainties; Li & Draine 2001; Zubko et al. 2004; Draine et al. 2007). We note that the dust mass derived for RXJ1131 is poorly constrained. If we adopt a dust mass from the other SED fit (i.e., without constraints at $24\,\mu m$), the dust mass would reduce by a factor of ~ 2.

There are a number of systematic uncertainties associated with this quantity. For instance, the mass opacity coefficient κ, the $\alpha_{\rm CO}$ conversion factor, and the bright-

ness temperature ratio r_{21}. If we instead use the "Galactic" α_{CO} value, which may be more appropriate for some ULIRGs (e.g., Papadopoulos et al. 2012) and minor mergers (Narayanan et al. 2012), the gas mass (and thus gas-to-dust ratio) would be ∼6 times higher. We note that this gas mass is physically feasible based on dynamical mass constraint. On the other hand, we would also obtain a higher gas mass if we assumed sub-thermal excitation between $CO(J = 2 \rightarrow 1)$ and $CO(J = 1 \rightarrow 0)$ emission, but we expect this to be a minor effect as CO emission in ULIRGs are thermalized up to $J = 3$ or 4. We also note that the gas-to-dust ratio derived for RXJ1131 maybe biased low as the gas is likely to be more extended than the dust. Consequently, the overall magnification factor for the CO gas may be lower than the optically thick dust, which dominates the far-IR luminosity, and thus leading to an overestimated dust mass via our adoption of the CO magnification factor.

5.5.4. *SFE and Depletion Timescales*

To first order, the star formation efficiency (SFE = L_{FIR} /M_{gas}) indicates the star formation rate per unit solar mass of molecular gas available in a galaxy. Using a wavelength range of $40 - 500\,\mu m$ defined in C13 as the far-IR luminosity, we find an SFE of $58 \pm 10\,L_\odot\,M_\odot^{-1}$, which is on the low end among other U/LIRGs at $z < 0.6$ (S97; Combes et al. 2011) but consistent with those of low-z spiral galaxies ($z < 0.1$; SV05) and high-z disk-like galaxies (Daddi et al. 2008). Assuming an α_{CO} of $0.8\,M_\odot$ (K km pc^2)$^{-1}$ is appropriate for RXJ1131, this would imply that it is converting gas into stars at an efficiency similar to those of "normal" star-forming disk-like galaxies rather than starburst galaxies (Tacconi et al. 2008; Riechers et al. 2011, C13). This is in agreement with its disk-like kinematic signatures.

Results from theoretical simulations have suggested that the disk component of a gas-rich progenitor galaxy can survive merging if it has a low star formation efficiency, which in turn reduces the gravitational torque available to remove the angular momentum of the gas, thereby allowing a higher gas fraction to be retained and redistributed over a large extent in the merged galaxy (Hopkins et al. 2009). With this, it is plausible that RXJ1131 will evolve into a disk galaxy with a small bulge component upon merging given its low SFE.

Assuming the star formation continues at the current rate without gas replenishment, this corresponds to a gas depletion time of $\tau = 102 \pm 25$ Myr. Since the star formation rate is expected to vary in an interacting system and AGN accretion also consumes some fraction of the gas, the depletion timescale should only be considered as an upper limit.

6. DISCUSSION

6.1. *Fate of RXS J1131−1231*

The classical picture for mergers is one where they are responsible for the formation of the local red and passive spheroidal galaxies. With more realistic treatments of star formation and feedback in recent simulations, it has been

suggested that it is possible to suppress bulge formation in gas-rich mergers, thereby forming large disks that resemble local spiral galaxies (Springel & Hernquist 2005; Robertson et al. 2006; Hopkins et al. 2009). The extended molecular gas distribution in RXJ1131 together with its low SFE implies that the removal of angular momentum of the gas via gravitational torque is inefficient. Other mechanisms e.g. bar-like structures that are more efficient at removing angular momentum will be required in order to transform the gas disk of RXJ1131 into a stellar spheroid and evolve into an E/S0 galaxy. Without these, it is more conceivable that RXJ1131 will retain its disk component and evolve into a disk galaxy upon its final coalescence with the companion.

6.2. *Velocity Offset and a Recoiling Black Hole*

Sluse et al. (2007, hereafter S07) report two sets of AGN lines observed in RXJ1131. The first set of lines is at $z \sim 0.653$, including the narrow component of the Balmer lines, the [OIII] 4959, 5007Å lines, and the MgII 2798Å absorption line; the second set is at $z \sim 0.658$, including the broad component of the Balmer lines and the MgII 2798Å emission line. Using the CO line center redshift as the systemic redshift, the second set of lines is blueshifted by ∼780 km s^{-1}. This implies that the broad line region (BLR) of the AGN is dynamically offset from the centroid of its host galaxy. We confirm this spatially in the channel maps in Figure 2 and Figure 7, where the line center of the CO gas is not co-spatial with the optical quasar — the point-like images along the lensing arc is offset to the NW of the CO line center emission. On the other hand, we find that the redshift of the [OIII] 4959, 5007Å lines tracing the narrow line region (NLR) is fully consistent with the systemic redshift, supporting previous claims that [OIII] 4959, 5007Å lines are good proxies to the true systemic redshift (e.g., Vrtilek 1985; Nelson 2000).

Large velocity offsets between emission lines of the BLR and the NLR may arise in a recoiling black hole (BH), where its BLR is moving at high velocity relative to the bulk of its host galaxy (Madau & Quataert 2004; Bonning et al. 2007; Loeb 2007). A recoiling black hole is expected when a pair of uneven mass BH coalesce, during which their orbital energy is being released as gravitational wave and a non-zero net angular momentum is being carried away. Depending on their initial conditions, numerical relativity simulations have shown that the recoil velocity can reach up to ∼4000 km s^{-1} for spinning BHs (e.g., Campanelli et al. 2007). Several sources have been proposed as recoiling BH candidates, such as CID-42 at $z = 0.359$ (Civano et al. 2010) and SDSS 0956+5127 at $z \sim 0.714$ (Steinhardt et al. 2012). One notable system is SDSSJ0927+2943 at $z \sim 0.713$, Komossa et al. (2008) suggest the possibility of a recoiling black hole in this system due to an offset of 2650 km s^{-1} between a set of narrow emission lines and a second set of broad Balmer and high-ionization forbidden lines. However, this scenario is refuted recently by Decarli et al. (2014), who confirm that the BLR lines in SDSSJ0927+2943 are consistent with the CO systemic redshift. This is in contrast with the case

in RXJ1131, our CO observations confirm the blueshifted BLR lines. The fact that the BH in RXJ1131 has a high spin parameter (Reis et al. 2014) renders the recoiling BH scenario a viable option for the origin of the blueshift. Since this model requires a merged BH, this interpretation would imply RXJ1131 have already encountered with the companion galaxy, which could explain the highly spinning BH observed in RX1131. In this picture, the presence of a nearby companion observed in our data may reflect that RXJ1131 is in its subsequent stages of (minor) merging resulting from previous passage of a major merger.

6.3. *The M_{BH}−M_{dyn} Relation*

Assuming RXJ1131 follows the local M_{BH}−M_{bulge} relation reported by Häring & Rix (2004), the virial-based black hole mass $M_{BH} \sim 8 \times 10^7\,M_\odot$ (Sluse et al. 2012) corresponds to a stellar bulge mass of $M_{bulge} = 5.4 \times 10^{10}\,M_\odot$. This implies that the bulge component is responsible for making up $\sim 65\%$ of the dynamical mass. If we subtract the black hole mass, gas mass, and dust mass[6] from the dynamical mass and ignore a contribution from the dark matter, this would yield an upper limit on the stellar mass of $6.8 \times 10^{10}\,M_\odot$. Thus, the bulge mass derived above based on the local relation is not unphysical. The stellar mass upper limit would also imply a lower limit on the M_{BH}/M_{bulge} ratio of $\sim 0.12\%$, which is consistent with the local relation within the scatter and with other intermediate-z radio-loud AGNs (McLure et al. 2006).

A dark matter fraction of over $f_{DM} \sim 0.5$ within the radius of which we used to derive the dynamical mass (i.e., $\lesssim 6$ kpc or $\sim 0.6 R_e$) would be required for RXJ1131 to lie above the local relation and fall outside the range of M_{BH}/M_{bulge} found in McLure et al. (2006), which is unlikely given its dynamical mass and rotation velocity (Courteau & Dutton 2015).

7. SUMMARY AND CONCLUSIONS

We present PdBI CO($J = 2 \to 1$) and CARMA CO($J = 3 \to 2$) observations toward the quadruply-imaged quasar RXJ1131 at $z_{CO} \sim 0.654$, benchmarking the first resolved CO imaging at intermediate redshift. We find a brightness temperature ratio of $r_{32} = 0.66 \pm 0.41$ between CO($J = 2 \to 1$) and CO($J = 3 \to 2$). Taking into account the large phase errors associated with CO($J = 3 \to 2$), this is consistent with thermalized excitation. We perform astrometric correction using archival VLA data, in which we detect continuum emission at 5 GHz in both the lensing galaxy and RXJ1131. In addition, we detect marginally resolved 2 mm continuum underlying the CO($J = 2 \to 1$) line in both galaxies.

We perform a lens modeling on different velocity channels of CO($J = 2 \to 1$) to study the intrinsic gas dynamics of RXJ1131. Our models indicate a CO-emitting source near RXJ1131, confirming the presence of an optically faint companion reported in previous studies (C06;

---

[6] Here, we adopt the lowest dust mass among the two SED models to derive an upper limit on the stellar mass. Since the dust mass only contributes a small fraction to the total mass, a factor of ~ 2 difference is minor.

B08). The source-plane positions form a symmetric velocity field, which is consistent with a kinematically-ordered disk galaxy. We find that the magnification factors vary from $\mu_L \sim 3$ to ~ 8 across different velocity channels, implying an extended gas distribution. Upon correcting for lensing magnification and subtracting a line flux contribution from the companion, we find an intrinsically symmetric double-horned line profile for RXJ1131. This together with the symmetric velocity gradient seen in both the source plane and the image plane strongly argues for a rotating disk morphology for RXJ1131, consistent with previous findings (C06). Assuming thermalized excitation and $\alpha_{CO} = 0.8\,M_\odot$ (K km pc^2)$^{-1}$, we find a lensing-corrected gas mass of $M_{gas} = (1.38 \pm 0.33) \times 10^{10}\,M_\odot$ for RXJ1131 and $(1.92 \pm 0.09) \times 10^9\,M_\odot$ for the companion. This implies a *gas* mass ratio of $\sim 7{:}1$. We derive a dynamical mass of $M_{dyn} = (8.3 \pm 1.9) \times 10^{10}\,M_\odot$ for RXJ1131 and $M_{dyn} \sin^2 30° \sim \mathrm{BLAH} \times 10^{BLAH}\,M_\odot$ for the companion. We thus find a gas mass fraction of ~ 0.19 for RXJ1131, confirming its gas-rich nature. The derived gas fraction is also consistent with the decreasing trend of molecular gas content since $z \sim 1.0$ (Combes et al. 2013). Owing to the lack of stringent constraints on the individual galaxy mass of RXJ1131 and the companion, we use their gas mass ratio to classify the system as a "wet" minor merger. We note that the merger system studied here is in stark contrast to the "wet-dry" merger SMM J094135+10277 at $z = 2.8$, where the quasar host galaxy harbors $\gtrsim 5$ times less gas mass than its companion (Riechers et al. 2013).

Fitting dust SED models to the submm photometry obtained with *Herschel* and additional IR photometry compiled from public catalogs, we derive a lensing-corrected dust mass of $M_{dust} = 4 \times 10^8\,M_\odot$ and a lensing-corrected IR luminosity of $L_{IR} \sim 1.5 \times 10^{12}\,L_\odot$, corresponding to a SFR$_{FIR}$ of $120 \pm 63\,M_\odot$ yr^{-1}. This implies that the merger system of RXJ1131 is dusty in nature with ongoing starbursts. **who contains the dust?** Comparing the gas and stellar distributions, we find that the CO gas is of similar spatial extent as the old and long-lasting stellar populations, whereas sites of recent star formation are embedded within the molecular gas reservoir. The starburst taking place in the inner few kpc is likely a consequence of gas accumulation driven by interactions with the companion. While properties such as CO linewidths, CO size, SFR, and gas mass found in RXJ1131 resemble local ULIRGs and high-z starbursts, its SFE is comparable to that of nearby and high-z disk-like galaxies rather than other ULIRGs. This is in agreement with its disk-like kinematic signatures. Theoretical simulations find that the disk component of a gas-rich progenitor galaxy with low SFE can be retained upon merging since the efficiency in removing angular momentum of the gas via gravitational torques provided by stellar components is reduced. Within this context, the extended molecular gas disk of RXJ1131 together with its low SFE implies that the nuclear starburst in RXJ1131 will buildup a larger bulge in the final product but is insufficient to transform into a E/S0 galaxy.

The optical BLR lines are blueshifted by $\sim 780\,\mathrm{km\,s^{-1}}$ from the systemic redshift, implying the AGN is offset from the dynamical center of its host galaxy. The offset could be the manifestation of a recoiling black hole in RXJ1131. Since this model requires a merged BH, this interpretation would imply RXJ1131 have already encountered with the companion galaxy, which would also explain the highly spinning black hole. Given the presence of the companion in the current data, RXJ1131 may be in its subsequent stages of minor merging from a previous major merger, as commonly predicted in simulations.

Our study here demonstrate the first resolved CO observations at intermediate redshift, allowing us to explore the $M_{\mathrm{BH}}-\sigma_*$ relation at $z\sim 0.65$ using dynamical constraints. We illustrate the use of gravitational lensing to allow for a detailed study of the ISM properties of a quasar host galaxy and a comparison of distributions between the dust, gas, and stars in the host galaxy despite emission of the quasar, and that dynamical lens modeling provides a promising avenue to study the gas kinematics and dynamics in distant quasar host galaxies. The first use of such technique is presented by Riechers et al. (2008), who reconstruct a velocity gradient and constrain the gas dynamics in the quasar PSS J2322+1944 at $z > 4$, which is the only other similar system where the emission of the host galaxy is lensed into an Einstein ring configuration. Similar resolved CO studies at intermediate redshift are needed to understand the co-evolution of SMBHs and their host galaxies through cosmic time.

Alexander, D. M., Brandt, W. N., Smail, I., et al. 2008, AJ, 135, 1968

Astropy Collaboration, Robitaille, T. P., Tollerud, E. J., et al. 2013, A&A, 558, A33

Bonning, E. W., Shields, G. A., & Salviander, S. 2007, ApJ, 666, L13

Borys, C., Smail, I., Chapman, S. C., et al. 2005, ApJ, 635, 853

Bothwell, M. S., Smail, I., Chapman, S. C., et al. 2013, MNRAS, 429, 3047

Brewer, B. J., & Lewis, G. F. 2008, MNRAS, 390, 39

Bussmann, R. S., Leung, T. K. D., & Conley, A. 2015a

Bussmann, R. S., Riechers, D., Fialkov, A., et al. 2015b, ApJ, 812, 43

Campanelli, M., Lousto, C. O., Zlochower, Y., & Merritt, D. 2007, Physical Review Letters, 98, 231102

Carilli, C. L., & Walter, F. 2013, ARA&A, 51, 105

Carpineti, A., Kaviraj, S., Darg, D., et al. 2012, MNRAS, 420, 2139

Carpineti, A., Kaviraj, S., Hyde, A. K., et al. 2015, A&A, 577, A119

Civano, F., Elvis, M., Lanzuisi, G., et al. 2010, ApJ, 717, 209

Claeskens, J.-F., Sluse, D., Riaud, P., & Surdej, J. 2006, A&A, 451, 865

Combes, F., García-Burillo, S., Braine, J., et al. 2011, A&A, 528, A124

—. 2013, A&A, 550, A41

Comerford, J. M., & Greene, J. E. 2014, ApJ, 789, 112

Coppin, K. E. K., Swinbank, A. M., Neri, R., et al. 2008, MNRAS, 389, 45

Courteau, S. 1997, AJ, 114, 2402

Courteau, S., & Dutton, A. A. 2015, ApJ, 801, L20

Courteau, S., & Rix, H.-W. 1997, in Bulletin of the American Astronomical Society, Vol. 29, American Astronomical Society Meeting Abstracts, 1332

Daddi, E., Dannerbauer, H., Elbaz, D., et al. 2008, ApJ, 673, L21

Daddi, E., Bournaud, F., Walter, F., et al. 2010, ApJ, 713, 686

Decarli, R., Dotti, M., Mazzucchelli, C., Montuori, C., & Volonteri, M. 2014, MNRAS, 445, 1558

Di Matteo, T., Springel, V., & Hernquist, L. 2005, Nature, 433, 604

Dowell, C. D., Conley, A., Glenn, J., et al. 2014, ApJ, 780, 75

Downes, D., & Solomon, P. M. 1998, ApJ, 507, 615

Draine, B. T., Dale, D. A., Bendo, G., et al. 2007, ApJ, 663, 866

Dunne, L., Eales, S. A., & Edmunds, M. G. 2003, MNRAS, 341, 589

Erb, D. K., Steidel, C. C., Shapley, A. E., et al. 2006, ApJ, 646, 107

Fazio, G. G., Hora, J. L., Allen, L. E., et al. 2004, ApJS, 154, 10

Gao, Y., & Solomon, P. M. 1999, ApJ, 512, L99

Greve, T. R., Bertoldi, F., Smail, I., et al. 2005, MNRAS, 359, 1165

Häring, N., & Rix, H.-W. 2004, ApJ, 604, L89

Hinshaw, G., Larson, D., Komatsu, E., et al. 2013, ApJS, 208, 19

Hopkins, A. M., & Beacom, J. F. 2006, ApJ, 651, 142

Hopkins, P. F., Cox, T. J., Younger, J. D., & Hernquist, L. 2009, ApJ, 691, 1168

Ivison, R. J., Papadopoulos, P. P., Smail, I., et al. 2011, MNRAS, 412, 1913

Iwasawa, K., Sanders, D. B., Teng, S. H., et al. 2011, A&A, 529, A106

Kennicutt, Jr., R. C. 1998, ARA&A, 36, 189

Komossa, S., Zhou, H., & Lu, H. 2008, ApJ, 678, L81

Larson, K. L., Sanders, D. B., Barnes, J. E., et al. 2016, ArXiv e-prints, arXiv:1605.05417

Li, A., & Draine, B. T. 2001, ApJ, 554, 778

Loeb, A. 2007, Physical Review Letters, 99, 041103

Madau, P., & Dickinson, M. 2014, Cosmic Star-Formation History

Madau, P., & Quataert, E. 2004, ApJ, 606, L17

Magorrian, J., Tremaine, S., Richstone, D., et al. 1998, AJ, 115, 2285

McLure, R. J., Jarvis, M. J., Targett, T. A., Dunlop, J. S., & Best, P. N. 2006, MNRAS, 368, 1395

Miller, S. H., Bundy, K., Sullivan, M., Ellis, R. S., & Treu, T. 2011, ApJ, 741, 115

Narayanan, D., Krumholz, M. R., Ostriker, E. C., & Hernquist, L. 2012, MNRAS, 421, 3127

Nelson, C. H. 2000, ApJ, 544, L91

Neugebauer, G., Habing, H. J., van Duinen, R., et al. 1984, ApJ, 278, L1

Ott, S. 2010, in Astronomical Society of the Pacific Conference Series, Vol. 434, Astronomical Data Analysis Software and Systems XIX, ed. Y. Mizumoto, K.-I. Morita, & M. Ohishi, 139

Papadopoulos, P. P., van der Werf, P., Xilouris, E., Isaak, K. G., & Gao, Y. 2012, ApJ, 751, 10

Peng, C. Y., Impey, C. D., Rix, H.-W., et al. 2006, ApJ, 649, 616

Pooley, D., Blackburne, J. A., Rappaport, S., & Schechter, P. L.

2007, ApJ, 661, 19

Puech, M., Flores, H., Hammer, F., et al. 2008, A&A, 484, 173

Reis, R. C., Reynolds, M. T., Miller, J. M., & Walton, D. J. 2014, Nature, 507, 207

Richards, G. T., Vanden Berk, D. E., Reichard, T. A., et al. 2002, AJ, 124, 1

Riechers, D. A., Hodge, J., Walter, F., Carilli, C. L., & Bertoldi, F. 2011, ApJ, 739, L31

Riechers, D. A., Walter, F., Brewer, B. J., et al. 2008, ApJ, 686, 851

Riechers, D. A., Bradford, C. M., Clements, D. L., et al. 2013, Nature, 496, 329

Rieke, G. H., Young, E. T., Engelbracht, C. W., et al. 2004, ApJS, 154, 25

Robertson, B., Bullock, J. S., Cox, T. J., et al. 2006, ApJ, 645, 986

Sajina, A., Yan, L., Fadda, D., Dasyra, K., & Huynh, M. 2012, ApJ, 757, 13

Salpeter, E. E. 1955, ApJ, 121, 161

Skrutskie, M. F., Cutri, R. M., Stiening, R., et al. 2006, AJ, 131, 1163

Sluse, D., Claeskens, J.-F., Hutsemékers, D., & Surdej, J. 2007, A&A, 468, 885

Sluse, D., Hutsemékers, D., Courbin, F., Meylan, G., & Wambsganss, J. 2012, A&A, 544, A62

Sluse, D., Surdej, J., Claeskens, J.-F., et al. 2003, A&A, 406, L43

Solomon, P. M., Downes, D., Radford, S. J. E., & Barrett, J. W. 1997, ApJ, 478, 144

Solomon, P. M., & Vanden Bout, P. A. 2005, ARA&A, 43, 677

Springel, V., & Hernquist, L. 2005, ApJ, 622, L9

Steinhardt, C. L., Schramm, M., Silverman, J. D., et al. 2012, ApJ, 759, 24

Stern, D., Eisenhardt, P., Gorjian, V., et al. 2005, ApJ, 631, 163

Tacconi, L. J., Genzel, R., Smail, I., et al. 2008, ApJ, 680, 246

Ueda, J., Iono, D., Yun, M. S., et al. 2014, ApJS, 214, 1

Vrtilek, J. M. 1985, ApJ, 294, 121

Walter, F., Carilli, C., Bertoldi, F., et al. 2004, ApJ, 615, L17

Walter, F., Decarli, R., Sargent, M., et al. 2014, ApJ, 782, 79

Wilson, C. D., Petitpas, G. R., Iono, D., et al. 2008, ApJS, 178, 189

Wright, E. L., Eisenhardt, P. R. M., Mainzer, A. K., et al. 2010, AJ, 140, 1868

Yuan, T.-T., Kewley, L. J., & Sanders, D. B. 2010, ApJ, 709, 884

Zubko, V., Dwek, E., & Arendt, R. G. 2004, ApJS, 152, 211